Digital Image Correlation under Scanning Electron Microscopy: Methodology and Validation

Adam D. Kammers[1] & Samantha Daly[1,2,*]

[1]*The University of Michigan Department of Mechanical Engineering, 2350 Hayward St., Ann Arbor, MI 48109*

[2]*The University of Michigan Department of Materials Science & Engineering, 2300 Hayward St., Ann Arbor, MI 48109*

*Corresponding Author: Samantha Daly

+1 (734) 763-8137

+1 (734) 647-9379

samdaly@umich.edu

The recent combination of scanning electron microscopy and digital image correlation (SEM-DIC) enables the experimental investigation of full-field deformations at much smaller length scales than is possible using optical digital image correlation methods. However, the high spatial resolution of SEM-DIC comes at the cost of complex image distortions, long image scan times that can capture gradients from stress relaxation, and a high noise sensitivity to SEM parameters. In this paper, it is shown that these sources of error can significantly impact the quality of the results and must be accounted for in order to perform accurate SEM-DIC experiments. An existing framework for distortion corrections is adapted to improve accuracy and the procedures are described in detail. As the results demonstrate, time varying drift distortion is a larger problem at high magnification while spatial distortion is more problematic at low magnification. Additionally, the new use of sample-independent calibration and a method to eliminate the detrimental effects of stress relaxation in the displacement fields prior to distortion correction are introduced. The impact of SEM settings on image noise is quantified and noise minimization schemes are examined. Finally, a uniaxial tension test on coarse-grained 1100-O aluminum is used to demonstrate these techniques, where active slip planes are identified and strain localization is examined in relation to the underlying microstructure.

Digital Image Correction, DIC, Scanning Electron Microscopy, SEM, Image Distortion, Deformation Mapping, Image Noise, Strain Localization

Introduction

The full-field, quantitative characterization of the small-scale deformation behavior of materials has recently been made possible with nanometer spatial resolution by using a combination of Scanning Electron Microscopy (SEM) and Digital Image Correlation (DIC), here termed SEM-DIC. SEM-DIC is an emerging and powerful technique used to study nano- and micro-scale phenomena in a wide range of materials. By combining SEM-DIC with electron backscatter diffraction (EBSD) microstructure mapping, it is now possible to link *in-situ* deformation behavior, at the length scale of the microstructure, directly to the underlying crystallography of the material (for detailed background information on the DIC and EBSD techniques, please see [1-5] and the references contained therein).

Recent work using SEM-DIC has provided substantially more information than possible with traditional methods, such as measuring the offset of fiducial lines on the surface. However, while high-quality examples of the application of SEM-DIC to experimental mechanics exist, few of them incorporate SEM image distortion corrections, which are significant. Recent experiments utilizing SEM-DIC include a 2011 study investigating damage mechanisms in porous carbonate under compressive loading [6]. In that work, the material had a small failure strain of 0.0011, yet strain localization was observed by keeping the noise levels sufficiently low through the use of a Field Emission Gun SEM (FEG-SEM), a large spot size, and long dwell times requiring up to seven minutes for a single image capture. While the SEM images used in that study were not corrected for distortion, displacement measurement uncertainties due to errors in positioning of the electron beam and image noise were examined by calculating the standard deviation from stationary image pairs. Experiments have also been conducted on metallic superalloys, including a 2009 work by Tschopp et al. on René 88DT utilizing a combination of EBSD, SEM, and DIC to relate strain localization directly to the Schmid factor of individual grains [7]. Tschopp et al. demonstrated that no relationship exists between the maximum shear strain and the Schmid factor for that material. In the *Experimental* section of this paper, it is demonstrated that dislocation slip is not always apparent in the shear strain field, but for the 1100 Al investigated here, there is a relationship between strain localization and Schmid factor. In 2012, Walley et al. used SEM-DIC to study the high temperature strain localization behavior of the nickel-based superalloy René 104 [8], and determined quantitative measures of strain localization that concentrated primarily at grain boundaries. While Walley et al. did examine the axial, transverse, and shear strain fields, no correlation was found between Schmid factor and strain localization. However, Walley et al. observed slip steps on the surface in grains with high Schmid factors, indicating that the spatial resolution of the DIC experiment may have been too low to capture slip displacements in this case. These works highlight the advantages and strong capabilities of this emerging approach, and the critical need for its careful development and accurate implementation.

The combination of SEM and DIC is a powerful new experimental methodology, but its correct implementation introduces challenges that are far more complex than those encountered in macro-scale DIC. The first challenge is the application of a suitable tracking pattern to the test sample surface. DIC measures displacements, and thus strains, by tracking a random, high contrast pattern from image to image. The pattern can be natural surface features, but more commonly is artificially applied. To achieve accurate results, it is important that a high-quality tracking pattern is used; incorrect results can often be traced back to a suboptimal pattern. Applying a small-scale tracking pattern, for example in a 50μm x 50μm or smaller field of view (FOV), is particularly difficult; because this has been addressed in recent work by the authors [9, 10] it will not be discussed here. Unlike macroscopic DIC, in which optical images can be fed directly into commercial correlation software, SEM-DIC also requires careful correction of a variety of distortions that are inherent to SEM imaging. Correction of these complex distortions, which arise from the rastering and time dependent nature of SEM image capture, the electromagnetic lenses, and the beam deflection coils, is another significant challenge of SEM-DIC. Due to their complexity, these distortions cannot be corrected by classical parametric distortion models. Extensive and high-quality work has been performed by Sutton et al. to account for these distortions [11-13], which can be considered as time varying drift and spatial distortions. Drift distortion dominates at high magnifications while spatial distortion dominates at low magnifications. Drift distortion can cause magnification-dependent pixel drifts as high as 0.34 pixels/minute at an image resolution of 29 nm/pixel as observed by the authors during the calibration phase of a tensile test on 1100 Al. Magnification dependent spatial distortions as high as 1.6 pixels at an image resolution of 730 nm/pixel can occur, as observed by the authors in a tensile test on pure Al at a global strain of 0.2. The distortions can result in largely inaccurate strain and displacement data, and it is critical that they are correctly accounted for when running SEM-DIC experiments.

This paper will begin by addressing SEM image distortion in the section titled *Distortion Corrections*. A distortion correction framework first developed by Sutton et al. [11-13] is adapted to correct for the effects of stress relaxation that occurs during the image scan and can be particularly detrimental to drift distortion correction. If stress relaxation is present and the drift distortion corrections do not account for it, it can contaminate the drift correction functions and surprisingly, lead to worse distortions than if the data was left uncorrected. In *Drift Distortion: Accounting for Stress Relaxation*, two methods for removing stress relaxation from calibration data are presented. Results from a test on 6061-T6 Al are discussed to illustrate the effects a large load drop of approximately 5 N between image scans can have on calibration image data. In addition to distortion, SEM images can suffer from substantially more noise than optical images [6, 12], which limits the minimum discernible displacement measurements. In the section *Noise Reduction*, the effect of SEM imaging parameters on the noise incurred in displacement fields is quantified. The noise comes from the statistical nature of the electron production from the gun and the interactions of these electrons with the sample, and thus is different for every pixel. In addition, the secondary or backscatter electron detector can generate noise and the circuitry within the SEM can then amplify this noise [14]. The dependence of SEM image noise on a wide range of parameter settings will be compared to noise from a Point Grey Grasshopper, Model 50S5M/C-C CCD commonly used for optical DIC experiments. In addition, the application of a local averaging filter to further reduce noise and enable the accurate identification of low-level initial strain localization will be discussed.

These approaches are then demonstrated with an in-situ tensile test on an 1100-O aluminum sample at an image resolution of 33 nm/pixel (67.4 μm horizontal field width (HFW)). Aluminum was chosen as a model material because it is known to deform primarily by slip on the {111} planes in the $<1\bar{1}0>$ directions. Deformation at the microstructural length scale is accurately tracked in real time during loading, and active slip planes are precisely determined through the combination of SEM-DIC and EBSD. The techniques described in this paper can be scaled up to larger FOVs, or down to smaller FOVs, as need dictates.

Distortion Corrections

The electromagnetic focusing and scanning systems of a SEM lead to complex image distortions, resulting in inaccurate DIC displacement data if left uncorrected. Sutton et al. [11-13]

were the first to recognize that these distortions exist and need to be corrected prior to displacement and strain calculations. These distortions are characterized into two categories – (1) drift distortion, which varies over time; and (2) spatial distortion, which is similar to the distortion present in optical lenses and can vary from test to test. The reader should keep in mind the critical fact that the spatial distortion of a point is directly related to the translation of that point. Note that the drift and spatial distortion correction techniques presented here have been applied to tests and verified to be effective at image resolutions from 29 to 1500 nm/pixel.

Pre-Test Calibration Phase

To correct for both spatial and temporal distortions, nominally eighteen micrographs of a speckle-patterned calibration sample are captured during a pre-test calibration phase [11]. A timer is started when the first image is captured, and the time at which every subsequent image is captured is recorded. The images are captured in pairs, with the sample remaining stationary within each pair. Between image pairs during this pre-test calibration phase, the sample is translated a known distance in the horizontal and vertical directions, as shown in figure 1. Four horizontal and vertical translations are performed to get an accurate measurement of spatial distortion and minimize the length of the calibration phase. The total x and y translation should be approximately 1/4 of the FOV. For example, in a 200 μm wide image, the total x and y translations would both be 50 μms and would be performed in 12.5 μm steps. Note that diagonal translations can also be made and used as a post-correction check to ensure that the sum of the horizontal and vertical spatial distortion surfaces account for the distortion seen in the diagonal translations. The stationary image pairs taken during pre-test calibration are used to correct for drift distortion, and the orthogonally translated images are used to correct for spatial distortion.

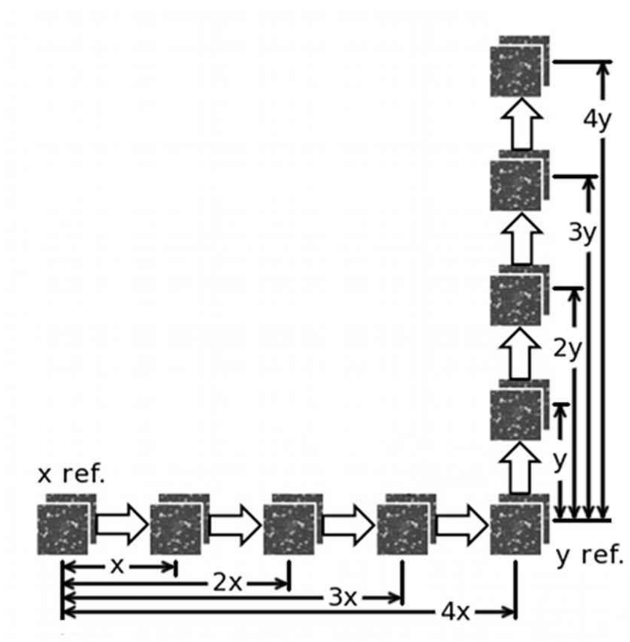

[**Fig 1** Diagram of the translation sequence used for distortion correction. Images are captured in pairs with translations occurring between stationary image pairs. The total x and y translation should be approximately 1/4 of the FOV.]

Test Calibration Phase

The duration of SEM-DIC tests can be on the order of several hours to a day, and although spatial distortion remains nominally constant, the drift distortion correction image pairs captured during the pre-test calibration phase may not accurately predict the drift distortion that occurs throughout the test. Thus, stationary calibration image pairs continue to be captured during the test phase. This requires that the chamber remains pumped at vacuum and the source energized following the calibration phase to avoid any effect on drift distortion from drops in chamber pressure or cooling of the source. Rigid body translations are not performed during the test, since spatial distortion does not vary throughout the test and can be accurately predicted during the calibration phase.

The effects of stress relaxation, if significant, become apparent in test phase calibration images captured of the loaded test sample surface. One method to remove stress relaxation from the test-phase calibration images, applicable at any image resolution, is through the use of an unloaded pattern (instead of the standard method of using the test sample pattern) for the image pairs captured during the test phase. If this is not possible, a relationship between load and relaxation can be determined and used for correction at image resolutions from 30 to 300 nm/pixel (verified in experiments). Both techniques are introduced in this paper. If stress relaxation is present and is unaccounted for, the distortion-corrected data can actually have a greater amount of distortion than the uncorrected data. In the work presented here, an unloaded patterned specimen of Inconel positioned next to the tensile specimen and at the same working distance was used, as shown in figure 2. More details on stress relaxation will be discussed in detail in the subsection *Drift Distortion: Accounting for Stress Relaxation*.

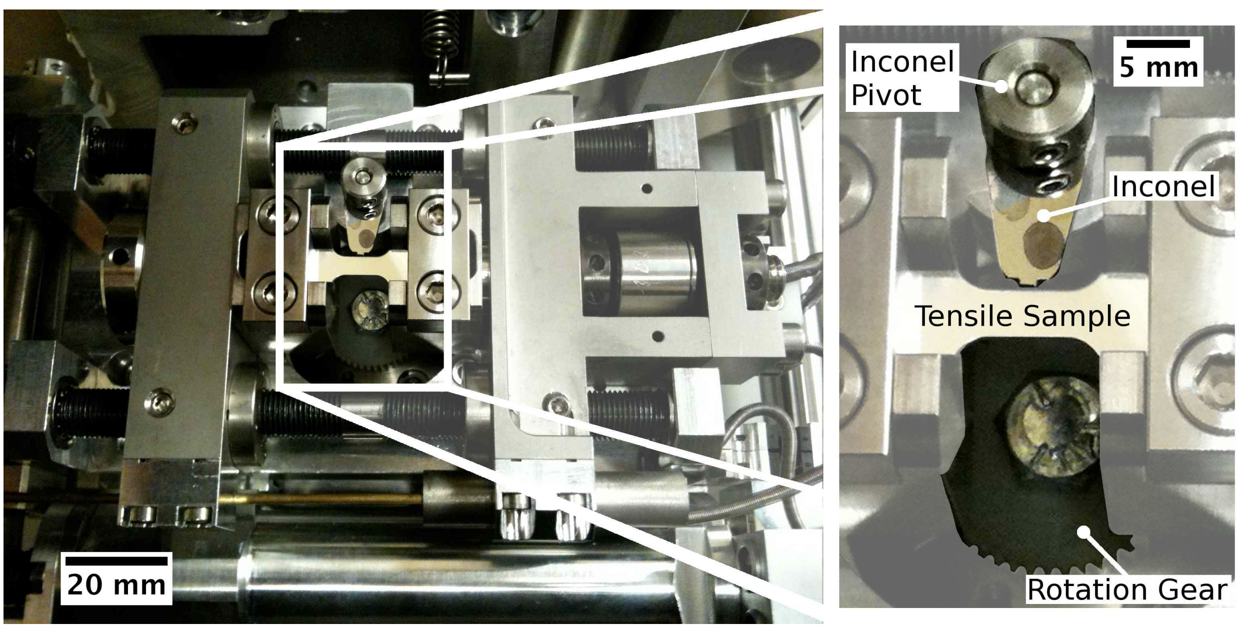

[**Fig 2** Grip section of the *in-situ* tensile stage, showing the aluminum tensile sample and Inconel sheet with a nanoparticle speckle pattern for sample-independent calibration, which improves distortion correction accuracy.]

Drift Distortions

Drift distortion (also known as pixel drift) can lead to significant errors over the typical duration of a SEM-DIC experiment. Drift distortion can result from motion of the SEM stage, heating of components in the electron column or the sample itself, charging of contamination on beam deflectors and apertures, charging of the SEM stage or sample, and interference from magnetic fields [15-20]. It is important to note that pixel drift is not constant within the image. At low magnifications with image resolutions coarser than approximately 750 nm/pixel, it will commonly appear as a vertical gradient in the displacement fields, while at higher magnification such as in the experiment presented here, it can have complex curvature as shown in figure 3. Drift distortion is related to the image resolution, and is more problematic in high spatial resolution experiments (particularly when the image resolution is finer than nominally 500 nm/pixel), as shown in figure 4. To generate figure 4, the magnitude of the mean drift velocity was calculated for each calibration phase stationary image pair in each test, and the largest magnitude value from each test was plotted. When converted to physical drift, the maximum pixel drift velocity is near 10 nm/minute for all image resolutions. Thus, the effect of pixel drift increases with magnification; for example, after one minute in a 1 mm HFW, a pixel will have drifted nominally 10 nm or 0.001% of the HFW. However, after one minute in a 10 μm HFW, a pixel will have drifted 10 nm, or 0.1% of the HFW. These drifts can add up over the typical duration of a SEM-DIC experiment. In a previous test with an image resolution of 29 nm/pixel (30 μm HFW), drift as high as 0.34 and 0.28 pixels/minute in the horizontal and vertical directions respectively was observed, which resulted in up to 14 (horizontal) and 68 (vertical) pixels of distortion in the final test images of the 4.5-hour experiment. Note that larger distortion was observed in the vertical direction for that test, because the vertical drift velocity remained nominally constant, whereas the horizontal distortion was initially high and then settled near zero (an occurrence specific to this test). In that previous test, the difference in vertical drift displacement over the entire final test image was approximately 13 pixels. If uncorrected, these

13 pixels constitute a significant displacement error which would have resulted in a vertical strain error of up to 0.014. In this work, image correlation (pre-correction) is performed on the stationary image pairs using a commercial software package [21], following which the relaxation-free displacement data is used to correct for drift distortion.

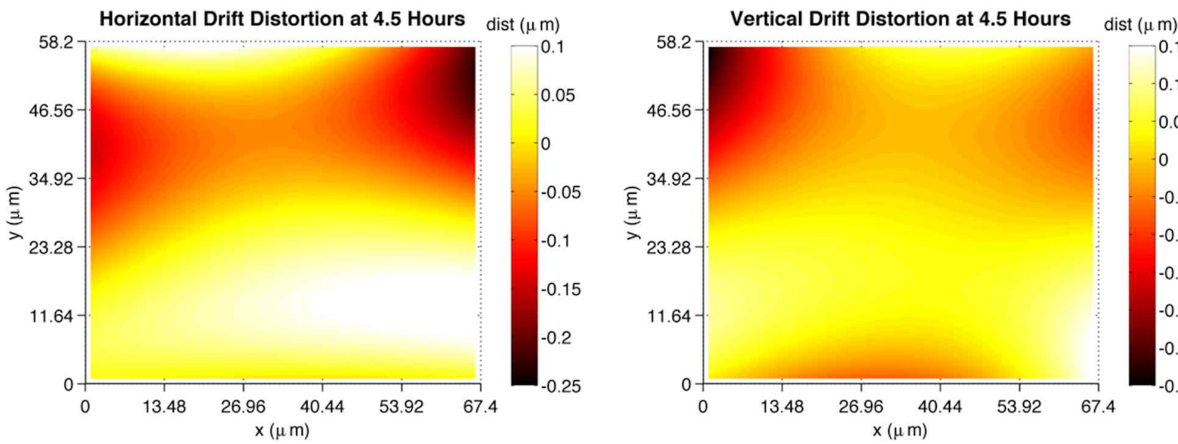

[**Fig 3** Drift distortion surfaces for the final test image of the 1100-O Al tensile sample presented in the *Experimental* section. These surfaces need to be subtracted from the horizontal and vertical displacement fields to correct for drift distortion.]

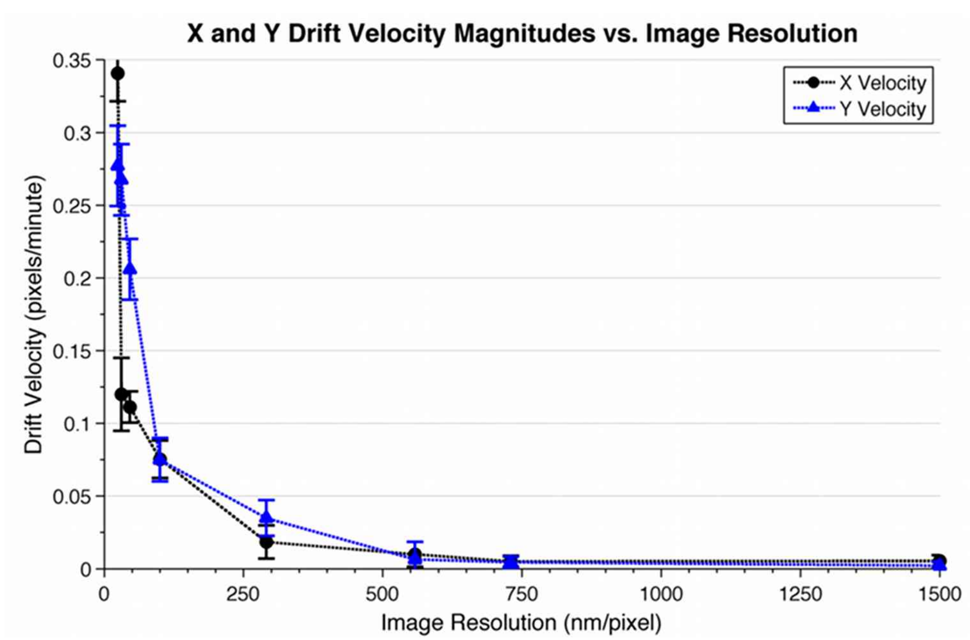

[**Fig 4** Drift velocity (in pixels/minute) decreases at coarser image resolutions (larger nm/pixel values), leveling out for image resolutions coarser than nominally 750 nm/pixel. When converting to physical drift, the max drift velocity at every image resolution is less than 10 nm/minute. Error bars represent the standard deviation.]

Drift Distortion: Accounting for Stress Relaxation

If the material being studied undergoes significant stress relaxation, drift distortion corrections performed without accounting for it can lead to greater distortions than if the images had been left uncorrected. Stress relaxation [22-24] exists in calibration image data captured during the test phase because SEM image capture proceeds by scanning an electron beam over the surface of a test sample, capturing each pixel sequentially (rather than simultaneously as with an optical camera). Long image scans are required in SEM-DIC to increase the signal to noise ratio, but can capture stress relaxation that occurs while the displacement is held constant for image acquisition. Figure 5 shows a plot of drift velocity versus time at one specific *(x,y)* position in the calibration images from a tensile test on 6061-T6 Al (horizontal tensile axis) at an image resolution of 68 nm/pixel (70 μm HFW). Here, the circles and triangles indicate drift velocity with and without stress relaxation correction, respectively. The uncorrected data (triangles) represent the drift velocities that would be used to correct for drift distortion without considering stress relaxation. The first 50 minutes represent the calibration phase, when the sample was under zero applied load and the drift velocity remained nominally centered around zero. After plastic deformation occurred at 135 minutes, the effect of stress relaxation on the displacement field became immediately apparent and the drift velocity rapidly increased. The stress relaxation in the sample, because it is a real deformation mechanism that was being artificially corrected for, caused a false increase in the drift velocity. The actual drift velocity, where stress relaxation is accounted for through the use of an unloaded calibration pattern, is shown by the circular data points in figure 5 and remained nominally constant as loading proceeded. This nominally constant drift velocity has been confirmed in additional tests with image resolutions ranging from 29 to 1500 nm/pixel.

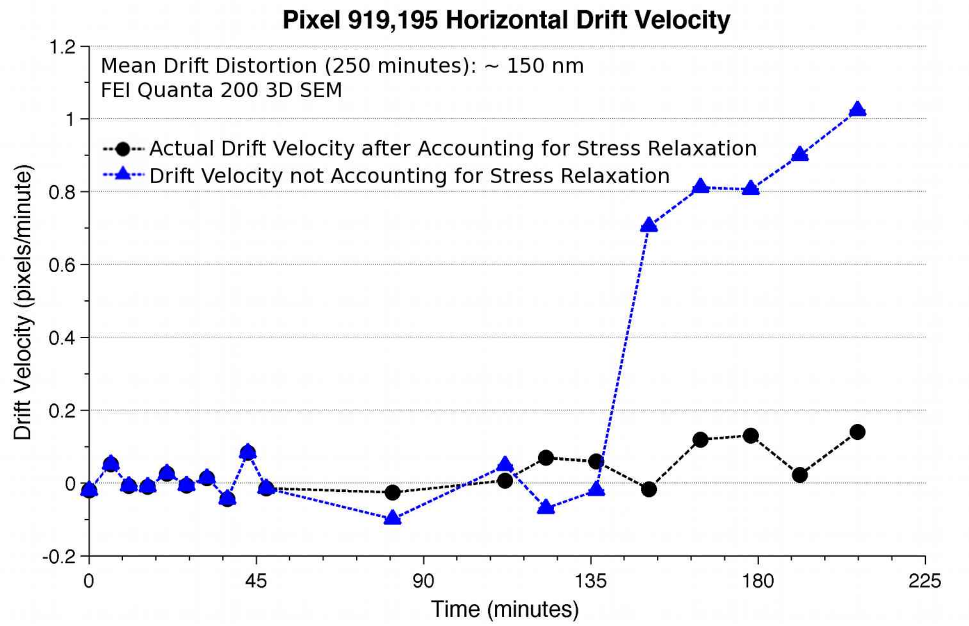

[**Fig 5** Trend in drift velocity at a specified pixel location throughout a test previously performed on 6061-T6 Al. Stress relaxation erroneously affects drift velocity and if not accounted for, will result in an overcorrection of the drift distortion. This test was performed at an image resolution of 68 nm/pixel (70 μm HFW) and a horizontal tensile axis.]

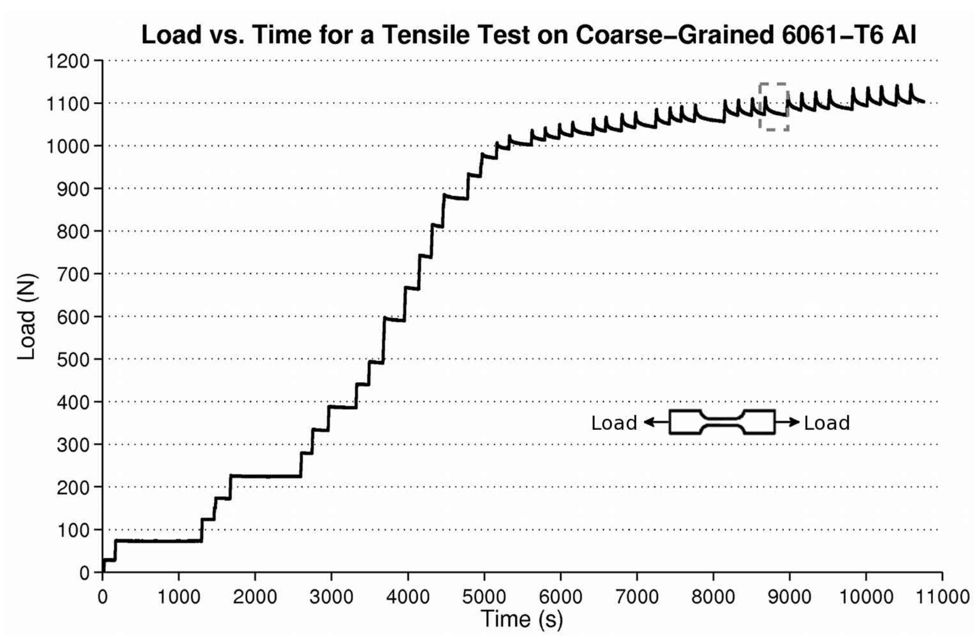

[**Fig 6** Load vs. time for a test on coarse-grained 6061-T6 Al. In the elastic regime, the load remains nearly constant during image capture. After plastic deformation occurs at ~5000 seconds, larger load drops during image capture are apparent.]

Large stress relaxation induced displacements in stationary calibration image pair data have been observed in both 6061-T6 coarse-grained aluminum and ultrafine-grained pure aluminum tensile samples when the load drop between image scans exceeds 1 N. If stress relaxation is observed in the calibration image pair data, it must be removed before the data is used for distortion correction. Consider as an illustrative example the load vs. time plot for a 6061-T6 Al test specimen tested at an image resolution of 68 nm/pixel (70 μm HFW) with a horizontal tensile axis, shown in figure 6. The stress relaxation occurring in the dashed box in figure 6, at nominally 9000 seconds, is clearly evident as a vertical gradient in the horizontal displacement field of the stationary calibration image pair captured during this time, shown in figure 7. Note, figure 7 has not been corrected for image distortion. However, drift and spatial distortion is very small. Spatial distortion scales with displacement and is near zero due to the small displacements observed here. Drift distortion is near 15 nm due to the short time between image captures; much smaller than the stress relaxation displacements. The relaxation rate was largest directly after loading stopped, and subsequently leveled as the displacement was held constant for image acquisition. The top of the image in figure 7 was measured to have shifted 180 nm to the right while the bottom of the image shifted by 60 nm. The horizontal displacements shown in figure 7 were much greater than those in the calibration phase stationary image pairs, which averaged 15 nm.

The large displacements caused by stress relaxation will lead to an overcorrection of drift distortion. Also, because relaxation results in larger magnitude displacements at the top of the image than at the bottom, the distortion of the displacement fields corrected with this data would spatially vary, incurring greater distortion at the top. As an additional complication, relaxation can occur either to the right or to the left in images, depending on the location of plastic deformation in the gage section. These jumps from positive to negative in apparent drift interfere with the generation of drift distortion correction functions and leads to increased distortion in the corrected data. Two techniques to remove stress relaxation effects, if observed in calibration image pairs captured during the test phase, are described below.

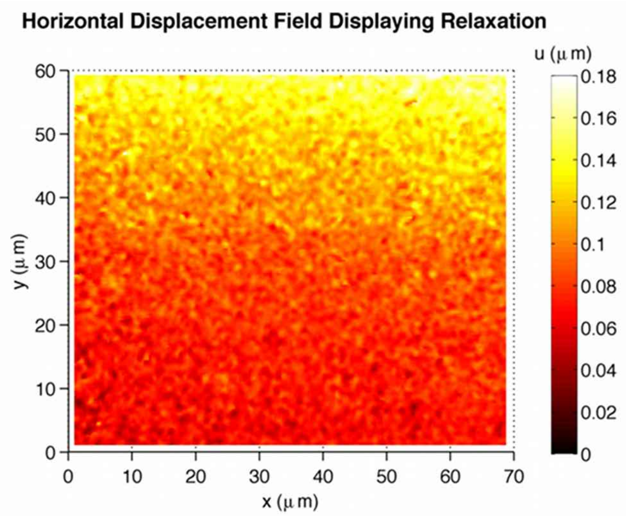

[**Fig 7** Horizontal (*u*) displacement field from the stationary image pair captured during the time period highlighted by the dotted box in figure 6. Stress relaxation of the 6061-T6 Al tensile sample occurred throughout the entire image scan, but at a greater rate initially than at the end.]

The first technique to remove stress relaxation from distortion corrected data, and the one used in the experiment presented later in this paper, utilizes an unloaded pattern on a separate substrate for calibration images. The unloaded calibration pattern is applied to an Inconel sheet and placed next to the tensile sample through the use of an ancillary positioning device as shown in figure 2. Inconel's resistance to creep and low coefficient of thermal expansion are particularly important for high temperature SEM-DIC testing. For convenience, the pattern does not need to be directly applied to the Inconel if the test is conducted at nominally ambient temperatures – it can instead be applied to a small piece of the test material attached to the top of the Inconel, allowing imaging of the tensile sample and the calibration pattern without adjusting contrast and brightness. The position of the calibration pattern can be adjusted with the ancillary positioning device controlled through the use of the SEM's external positioning knobs, using z-control to locate the pattern at the exact working distance of the tensile sample and rotation control to locate the pattern away from the heating element used in high temperature tests as further protection against creep. The ancillary positioning device is mounted directly to the tensile stage so that when calibration images are needed, the x and y stage positioning knobs can be used to translate from the tensile sample to the calibration pattern. Note that the test sample pattern can be used during the (unloaded) calibration phase, but the unloaded pattern should be used after loading of the sample begins.

If stress relaxation is apparent and hardware modifications cannot be made to the SEM or tensile stage for use of an unloaded pattern, linking of the relaxation-induced displacement to the load drop that occurs during the calibration image scans can be used. This technique has been validated with experiments at image resolutions from 30 to 300 nm/pixel. Figure 8 shows the load drop that occurred due to stress relaxation during the capture of the stationary calibration image pair in the highlighted area of figure 6. The top curve shows the load profile for the first image scan and the lower curve shows the load profile for the second image scan. Since the time each pixel is scanned is known, surfaces are created consisting of the load at each pixel in each scan. The surface from the second scan is then subtracted from that of the first in order to reveal the change in load that occurred at every pixel between the first and second image, as shown in figure 9. As expected, the load drop surface in figure 9 shows a similar gradient to the horizontal displacement field in figure 7. (Note that if the relaxation is to the left, causing the displacement to be initially negative and increase over the scan, the load data can be flipped so that both load and displacement data increase over the scan). The load drop surfaces are then converted to displacement surfaces and aligned with the horizontal (*u*) displacement fields through the application of a conversion factor. The conversion factor is determined by finding the value that, when multiplied by the load surface, minimized the difference between all of the *u* displacement fields and their associated load surfaces. For the 6061-T6 Al test and sample geometry considered here, the conversion factor was found to be 0.024 μm/N. The conversion factor is applied to the load surfaces, and the converted surfaces are subtracted from the *u* displacement fields. The displacement field from figure 7 is shown in figure 10 after relaxation has been removed. The remaining curvature of the displacement field is due to drift and spatial distortions and can now be removed with subsequent distortion correction. This technique was initially developed for single image scans but has also been applied to integrated image scans, in which image integration is used to further reduce data noise. To correct integrated images, the load drop that occurs over each image scan is calculated and then averaged. In the integrated images, relaxation is still observed in the horizontal displacement fields for a horizontal tensile axis, but the magnitude is reduced. This technique can also be applied to images in which the tensile axis is vertical. Then relaxation will be observed in the vertical displacement field with a vertical gradient similar to that shown in figure 7.

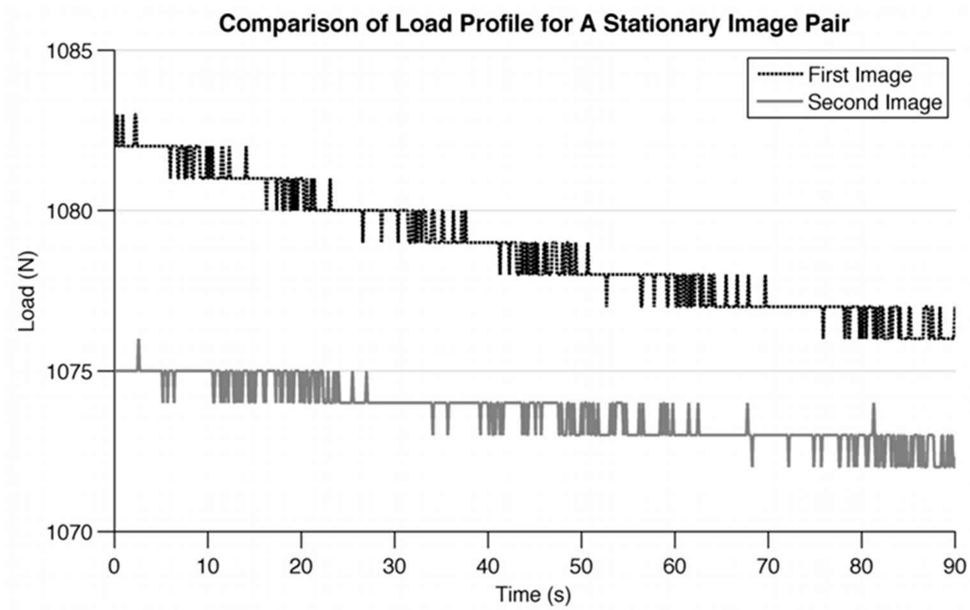

[**Fig 8** Load drop that occurred for the stationary image pair captured of the 6061-T6 Al tensile sample during the highlighted period shown in figure 6.]

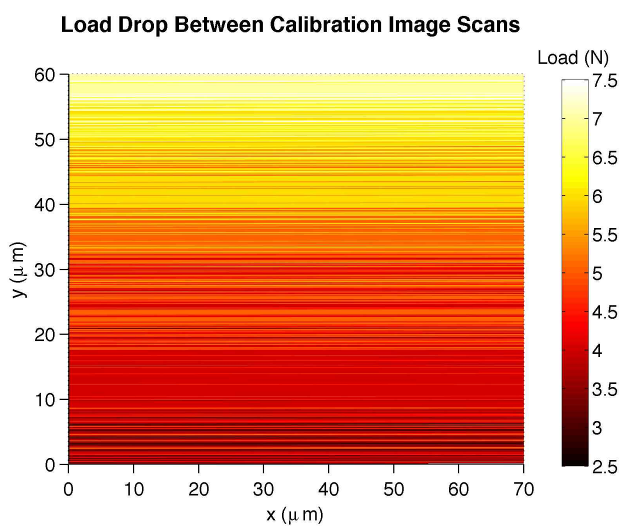

[**Fig 9** Surface representation of the load drop that occurred between the first and second image captured of the 6061-T6 Al tensile sample during the highlighted period shown in figure 6.]

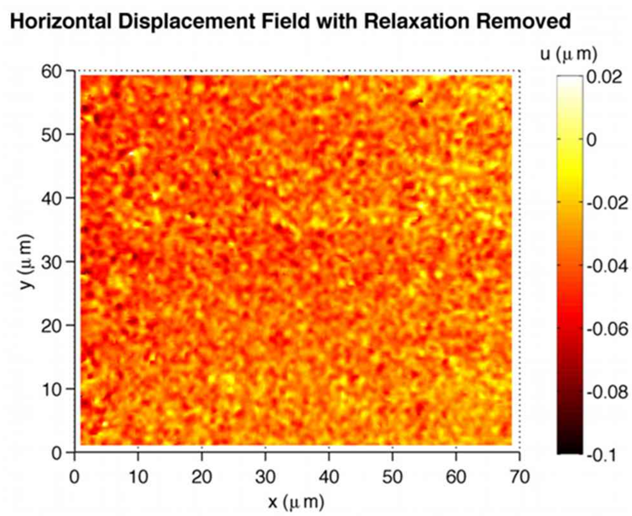

[**Fig 10** Displacement field of the 6061-T6 Al tensile sample from figure 7 after displacements due to relaxation have been removed. The remaining curvature of the displacement field is due to drift and spatial distortions and can now be removed with subsequent distortion correction.]

Both of the approaches discussed above effectively remove the effects of stress relaxation from calibration image data, but the user must decide which technique to implement. An unloaded pattern can be used at any image resolution and is the easiest to implement if it is possible to make minor modifications to the SEM or tensile/compression stage. Since the unloaded pattern calibration images do not suffer from stress relaxation, their DIC data can be used as-is for distortion correction. Relating relaxation displacements to the load drop allows for quantification of the stress relaxation, but adds the additional step of correcting the calibration data for relaxation prior to using it for distortion correction. However, since the relationship between load drop and stress relaxation displacements is known, application of this technique does allow for the removal of stress relaxation from test image data. This technique has only been validated in experiments from 30 to 300 nm/pixel. At image resolutions coarser than 300 nm/pixel, stress relaxation displacements are of very small magnitude and have not been observed. Additionally, note that the conversion factor changes with material, sample geometry, and number of image integrations. For example, in tests performed on ultrafine-grained pure Al using four image integrations at an image resolution of 31 nm/pixel (110 μm HFW), the conversion factor was found to be 0.06 μm/N versus 0.024 μm/N for the single scans of 6061-T6 Al presented here. Variations in the relaxing displacement fields at areas of strain localization could not be observed. Additionally, stress relaxation was not observed in 1100-O Al tensile tests at image resolutions of 29 and 33 nm/pixel where the load drop between test-phase calibration image pairs never exceeded 1 N. Based on ease of implementation and simplicity, unless the user desires to quantify stress relaxation, the use of an unloaded pattern is recommended.

Spatial Distortions

Spatial distortions can cause large errors in the calculated displacement fields, particularly in high strain or large displacement tests. For example, spatial distortions of 1.60 pixels (in the tensile direction) were observed in pure aluminum samples at a strain of 0.2 for an image resolution of 700 nm/pixel (720 μm HFW). Spatial distortion is similar to the distortion present in optical lenses, but it cannot be corrected with classical parametric distortion models due to the complex electromagnetic focusing and scanning processes utilized in an SEM. While spatial distortion remains nominally constant throughout a test, it has been observed to change between tests due to filament replacement, gun or aperture alignments, or other service performed on the electron column. In this work, it has been observed that spatial distortion decreases as magnification increases.

Spatial distortion is itself a function of displacement, and thus can be quantified from translated image pairs captured during the calibration phase and does not require any additional translated image pairs to be captured during the test. As mentioned previously and as outlined in [11], during the calibration phase the sample is translated by known amounts in x (u displacement) and y (v displacement). These displacements are sized so that the total translation in each direction is greater than that expected during the test. In this work, a total translation of approximately 1/4 of the FOV size is used. Using the image just prior to the first translation in each direction as a reference (*x ref* and *y ref* in figure 1), digital image correlation is performed on the first image captured after each translation. This results in data sets composed of displacement fields for pure *u* and *v* displacements of varying magnitude (x, 2x, 3x, 4x and y, 2y, 3y, 4y as shown in figure 1).

Prior to being used for spatial distortion correction, the translated DIC data is corrected for drift distortion using the functions generated from the stationary image pairs. Next, the input rigid body displacements are subtracted from each data set. If undistorted, the resulting *u* and *v* displacement fields would be centered at zero. Therefore any nonzero displacement data points are a result of spatial distortion (and image noise, which must be minimized). The spatially distorted *u* and *v* displacement fields are then fit with biquintic surfaces, as shown in figure 11 for the test presented in the *Experimental* section of this paper. These surfaces represent the spatial distortion for the given input translations and change based on translation direction and magnitude as demonstrated in figures 11 and 12 respectively. Spatial distortion surfaces for 10 μm horizontal and vertical translations are shown as examples in figure 11. Figure 11a (11b) represents the *u* (*v*) spatial distortion for a 10 μm displacement in only the *x* (*y*) direction. Figure 11c (11d) shows the *u* (*v*) spatial distortion for a 10 μm displacement in only the *y* (*x*) direction. If the sample was translated 10 μms in both the *x* and *y* directions, the *u* (*v*) spatial distortion would be the sum of figure 11a and 11c (figure 11b and 11d) as shown in figure 11e (11f). Surfaces similar to those shown in figure 11 exist for each input translation. A trend in the curvature of these surfaces with the input rigid body translation will be apparent and will be used in the following steps to correct for spatial distortion.

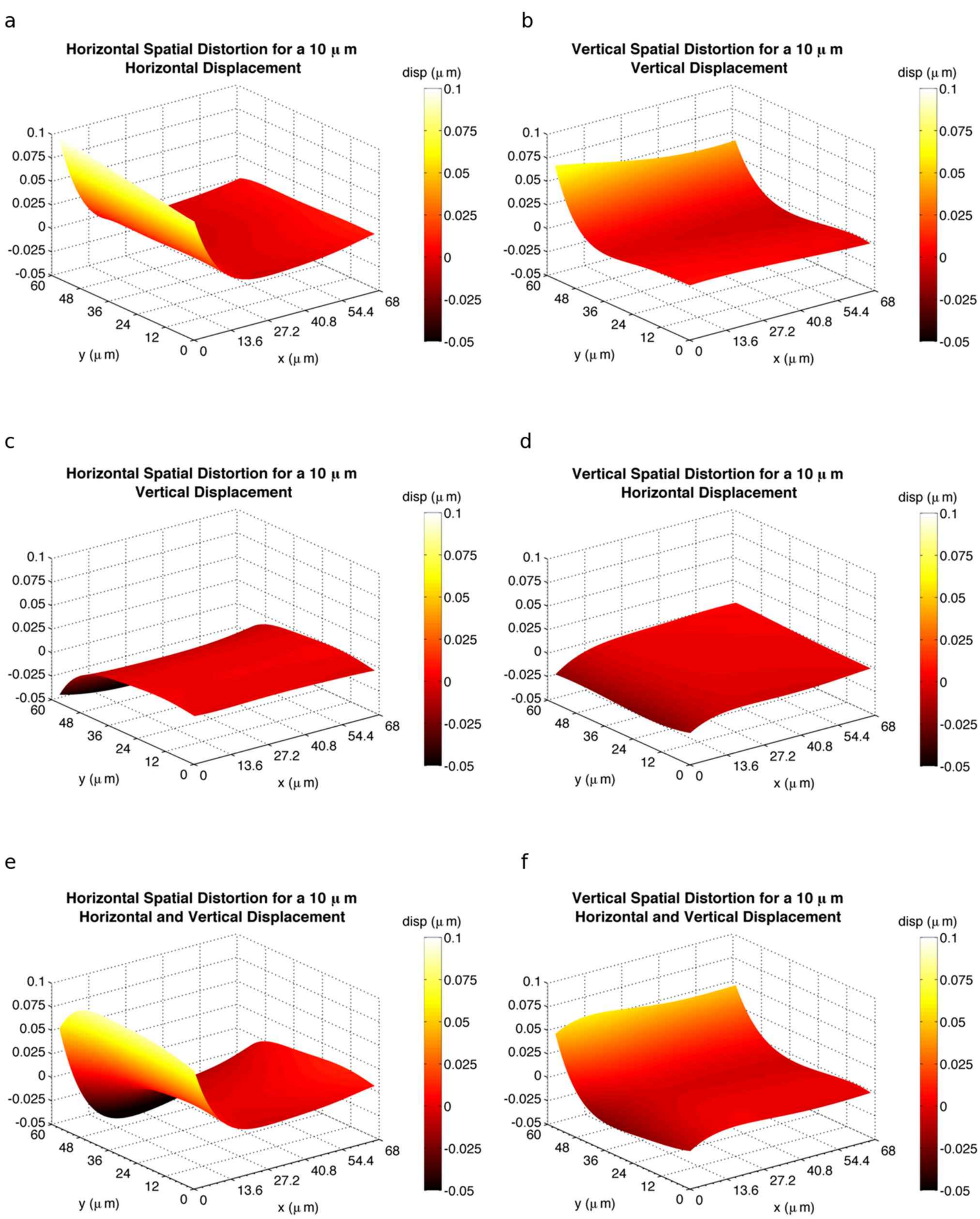

[**Fig 11** Spatial distortion surfaces for 10 μm horizontal and vertical displacements. These surfaces were obtained from the test on 1100-O Al presented in the *Experimental* section at an image resolution of 33 nm/pixel (67.4 μm HFW). Note that these surfaces scale with input translation.]

A linear relationship between spatial distortion and input translation is evident at all data points. After obtaining the spatial distortion surfaces for each rigid body translation, the spatial distortion at each individual data point is plotted against the input translation value, as shown in figure 12. At each data point, this yields four linear functions unique to that data point (*u* and *v* distortions for displacements in the *x* direction, and *u* and *v* distortions for displacements in the *y* direction). Figure 12 shows the *u* distortion and *v* distortion data and linear best-fit curves for a series of translations in the *x* direction.

Once these four functions are determined *for every data point*, the spatial distortion in each test image is removed by entering the *u* and *v* displacement at each data point into the spatial distortion linear functions for that specific point. The linear functions yield unique *u* and *v* spatial distortion fields that are subtracted from the drift distortion corrected displacement fields.

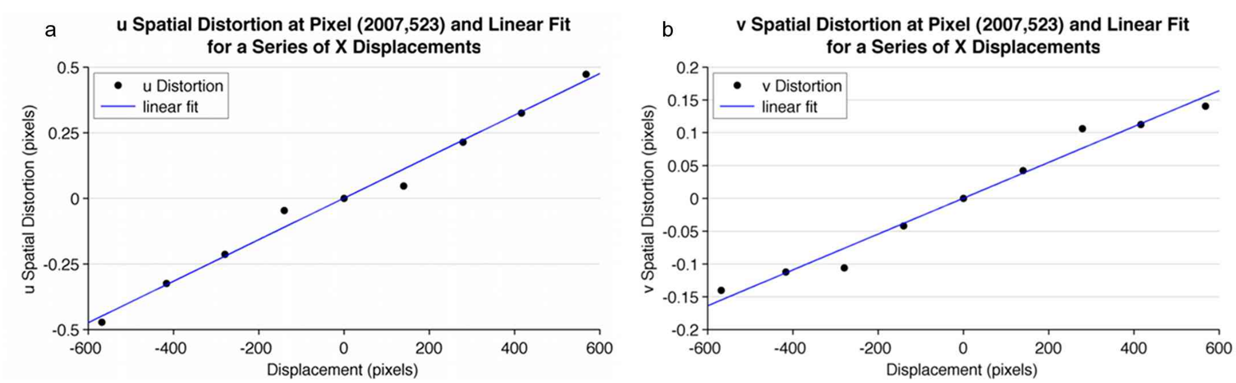

[**Fig 12** Spatial distortion at pixel location (2007,523) and linear curve fit for a series of translations in the *x* direction for the 33 nm/pixel image resolution (67.4 µm HFW) experiment on 1100-O Al presented in the *Experimental* section.]

Noise Reduction

In this section, guidelines for improving the signal to noise ratio in SEM-DIC will be described. SEM imaging parameters must be carefully selected to obtain micrographs with low levels of noise, a particularly important consideration when handling brittle materials or examining low strain phenomena. Several of these guidelines are also applicable to the reduction of noise at high temperature in-SEM testing, but specialized modifications for high temperature applications (validated up to 800°C) are necessary and will be described in future work.

Drift and spatial distortion corrections are necessary, but have minimal effect on the amount of random, SEM-introduced noise inherent in the displacement fields. A general guideline for minimizing SEM image noise is to use a long dwell time and high beam current. Image integration, in which multiple images are captured and the grayscale value at every pixel is averaged over all of the images, is also effective in reducing image noise [12]. This comes from the fact that the noise distribution is random and thus will not be at the same location in each scan, causing it to be of a reduced magnitude in the final averaged image. However, care must be taken when using image integration to avoid capturing images when stress relaxation is causing the load to drop rapidly, as sample motion can cause blurring of the resulting image and reduced correlation accuracy. Noise reduction through image integration is also possible with optical CCDs, but is often not utilized since it would require loading to be paused and thus is not included in this comparison.

Noise in SEM-DIC data can be quite large and has a strong dependence on imaging parameters, but with careful experimentation it is possible to reduce SEM noise greatly, to levels below those observed in a Point Grey Grasshopper, Model 50S5M/C-C CCD, commonly used for optical DIC. Figure 13 compares standard deviations in the SEM-DIC displacement field across a wide range of different imaging parameters. The SEM images in this plot were captured with the secondary electron detector in a FEI QUANTA 200 3D SEM with a tungsten filament, working distance of 16mm, and an image resolution of 500 nm/pixel (500 μm HFW). The pattern was created with drop-cast gold nanoparticles and a 15 x 15 pixel subset (subset size selected to contain on average 9 speckles) and a three-pixel step size were used for correlation. For the purposes of this comparison, a low magnification was used to avoid the image shifts commonly observed at higher magnifications in single image scans [12]. These image shifts appear at HFWs smaller than approximately 100 μms as horizontal bands of abrupt changes in displacement in both the u and v displacement fields. Since the location and width of these bands change from scan to scan, image integration is effective at removing them and must be used at smaller HFWs. It is important to note that CCD images do not suffer from these image shifts.

The displacement noise for a commonly used optical CCD (Point Grey Grasshopper, Model 50S5M/C-C, 2448x2048 pixel resolution) was calculated as a comparison to the data presented in figure 13. The speckle pattern for the optical DIC data was created by coating the sample with Golden Airbrush Titanium White paint #8380 and then overspraying it with Golden Airbrush Carbon Black paint #8040 from an airbrush (model Iwata Custom Micron B). DIC was performed using a subset size of 21 x 21 pixels and step size of 3 pixels (subset size selected to contain on average 9 speckles). Prior to comparison, both the SEM and CCD images were trimmed so that 80,000 data points were analyzed.

As apparent in figure 13, SEM image noise is reduced with a larger spot size, longer dwell time, and more image integrations. The smallest standard deviations of 0.0092 pixels in the horizontal direction and 0.0087 pixels in the vertical direction were achieved at a 20 kV accelerating voltage, 1.2 nA beam current, and 10 microsecond dwell with 8 image integrations. These images took 72.42 seconds to capture and had less noise than images that took over twice the time to capture. These SEM noise levels are both smaller than those of the Grasshopper CCD with horizontal and vertical standard deviations of 0.0126 and 0.0099 pixels respectively. While the data presented in figure 13 is from a tungsten filament SEM, displacement noise from images captured in a Philips XL30 FEG-SEM was also minimized with low voltage, high beam current, long dwell time, and image integration. Typically, noise levels in a FEG-SEM will be lower than those in a tungsten filament SEM due to the higher brightness and lower energy spread of the field emission source compared to the tungsten filament. The reader should note that the noise characteristics of the Point Grey Grasshopper CCD do not necessarily represent the noise present in other optical imaging systems. Optical noise levels lower than the SEM noise stated here may be achieved with different CCD or CMOS systems through cooling of the chip and/or image integration.

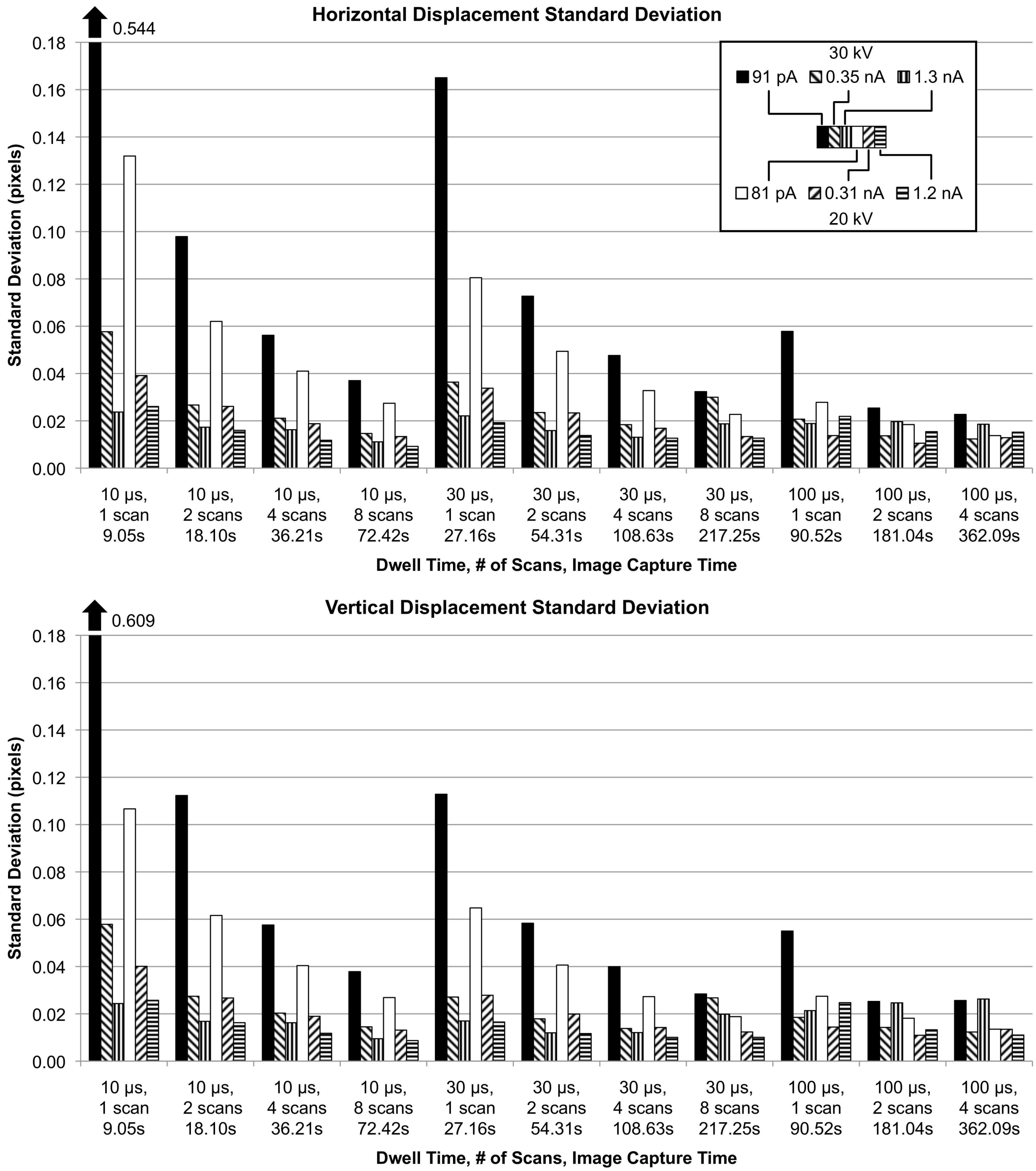

[**Fig 13** Standard deviations in the SEM-DIC displacement fields for different imaging parameters. Noise is minimized by using a 1.2/1.3 nA beam current, 10 micosecond dwell time, and 8 image scans for a total image scan time of 72.42 seconds. In general, increasing beam current and dwell time reduces image noise. (81/91 pA = spot size 3, 0.31/0.35 nA = spot size 4, and 1.2/1.3 nA = spot size 5)]

At low strain values, noise in the displacement and strain fields can hide true displacement and strain localization. In these cases, a local averaging filter is useful to make areas of localization apparent. Application of the filter will blend the strain values so they will be of a reduced magnitude; therefore, this approach is not appropriate for obtaining quantitative values of small strains, but rather as a method to pinpoint initial localization. The averaging filter box should be sized to contain both the high value (peak) and neighboring low value (valley) of noise to effectively cancel them out. If the size of the filter box is too small to capture at least one noise peak and valley, the data will not be smoothed. Conversely, an oversized filter box containing numerous peaks and valleys may smooth the data more than desired. Figure 14a shows an axial strain field from the tensile test presented in the *Experimental* section where high levels of noise make strain localization difficult to discern. It also shows the noise observed in the axial strain field from stationary image pairs captured during this test. This 'noise threshold', peaks at strains of 0.030 while the axial strain field peaks at only 0.050, making it difficult to identify strain localization. Figure 14b shows the same strain and noise fields after a 95x95 pixel (3.13x3.13 μm) averaging filter represented by the box at the top left of the strain field in figure 14a has been applied to the data. The averaging filter reassigns the value of each data point with the average value of its neighbors. The size of the neighborhood is specified by the size of the filter box. After application of the averaging filter, the noise peaks are now 0.004 while the peaks from the actual strain field are 0.012, making it easier to identify strain localization. This initial strain localization matches up with the axial strain maps from higher loads shown in figure 17. This technique is useful for identifying the relationship between initial strain localization and specific areas of the microstructure.

SEM-DIC data also experiences an interpolation bias [3,25] that shows up as regular vertical (horizontal) lines in the horizontal (vertical) displacement and strain fields. These lines can disguise actual displacement and strain data at low strain values, but can be reduced by using higher order interpolation filters [25]. Additionally, a smooth transition from black to white in the speckle pattern or the application of a low-pass filter to DIC images will reduce interpolation bias [25]. This interpolation bias is often easy to recognize and does not interfere with the identification of strain localization.

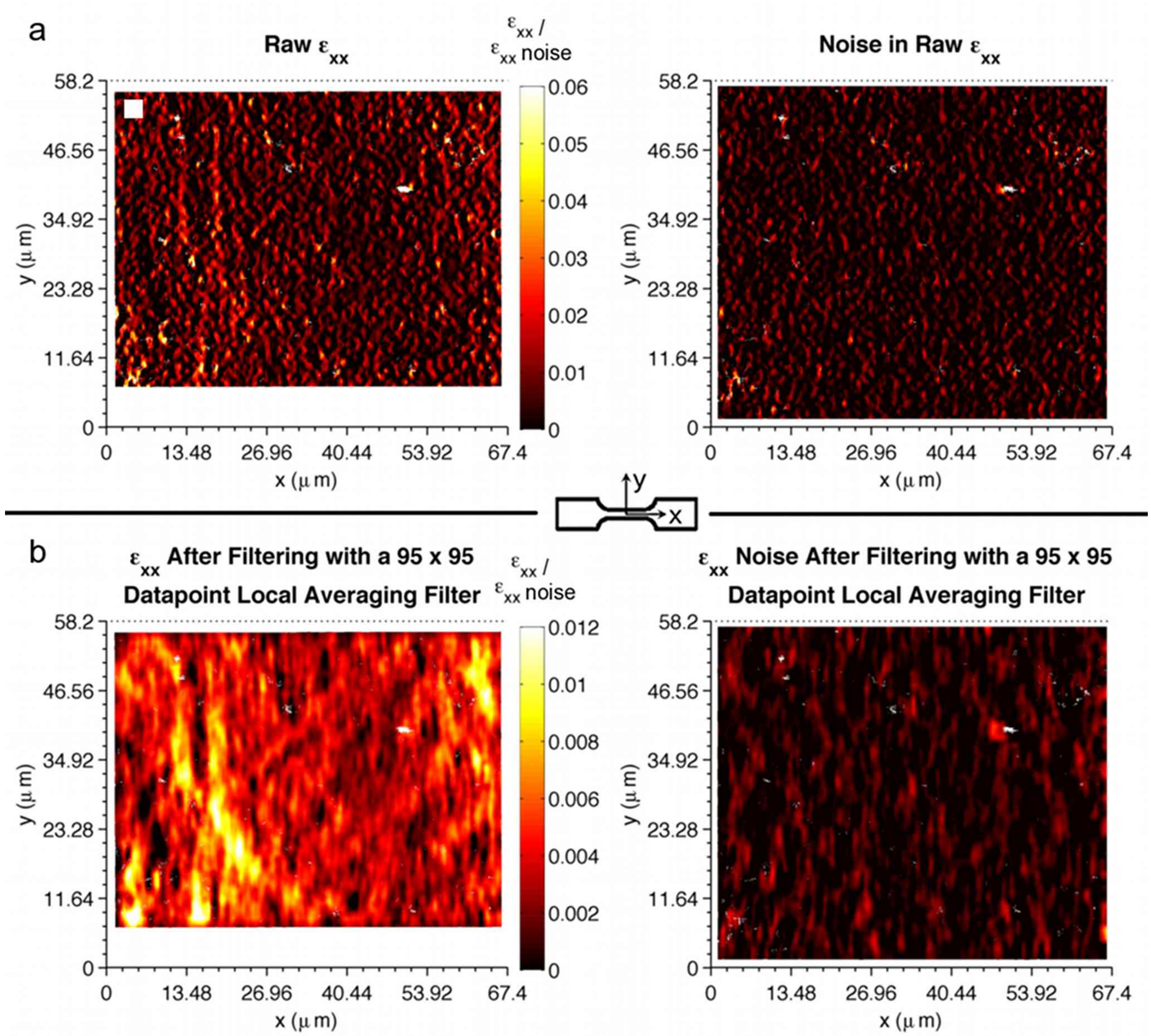

[**Fig 14** Axial strain fields at a globally applied strain of 0.004 for the tensile test on 1100-O Al presented in the *Experimental* section. (a) shows the raw axial strain field as well as the axial strain noise field observed in stationary calibration image pairs. The high noise level makes identifying strain localization a challenge. (b) shows the same strain field and noise field after the application of a 95x95 pixel averaging filter denoted by the white box in the axial strain field in (a). Strain localization now stands out from the noise and can be observed in later axial strain fields shown in figure 17.]

Experimental

Using the techniques described in this paper, an *in-situ* tensile test was performed on 1100-O aluminum. The material was purchased in sheet form from McMaster-Carr. Dogbone-shaped tensile test specimens with a gage cross-section of 2 mm x 1 mm and a length of 8 mm were fabricated by electro-discharge machining. The 4:1 gage length to width ratio allows for the gage section to be subjected to pure tension to achieve an accurate reflection of the material's constitutive behavior [26]. Samples were ground and polished starting by first grinding the edges of the gage section with 15 μm silicon carbide abrasive papers to remove edge roughness created by electro-discharge machining. One face of the sample was then mechanically polished with 400, 600 and 800 grit SiC papers with deionized (DI) water. Buehler MetaDi supreme polycrystalline diamond suspensions were then used, starting at a grit size of 9 μm, followed by 3 and 1 μm. Polishing was finished with a final abrasive of 20 nm colloidal silica on a neoprene-style Mager Scientific Dura Chem PC-740 cloth. Polishing resulted in a final gage cross section of 2 mm x 0.88 mm. Platinum markers (500 nm diameter x 500 nm tall) were deposited on the surface of the sample with a focused ion beam (30kV accelerating voltage, 10 pA beam current) to mark the test FOV, as shown in figure 15. A grid of markers was used so that EBSD could be performed on numerous potential test FOVs. EBSD (settings: 25 kV, spot 6, step 500 nm) was performed on the polished side of the sample to create an accurate microstructural representation of the test FOV. Care was taken to accurately align the EBSD FOV with the test FOV so that the two datasets could be overlaid for analysis. Prior to performing the EBSD scan, the sample was rotated such that the outlined area was centered in the scan in the EBSD data collection software user interface, and lines connecting neighboring markers were parallel to the x- and y-axes. To ensure alignment in the DIC reference image, these same conditions were again checked. If the two fields of view are not aligned properly, the resulting images and underlying data will need to be stretched or distorted until the markers in the images generated from the EBSD data are aligned with the markers visible in the DIC reference image. While stretching the images is straightforward, it will lead to inaccurate Euler angles unless the data is manipulated as well. Following EBSD, one side of the sample was patterned by self-assembly of 70 nm diameter gold nanoparticles as described in [10].

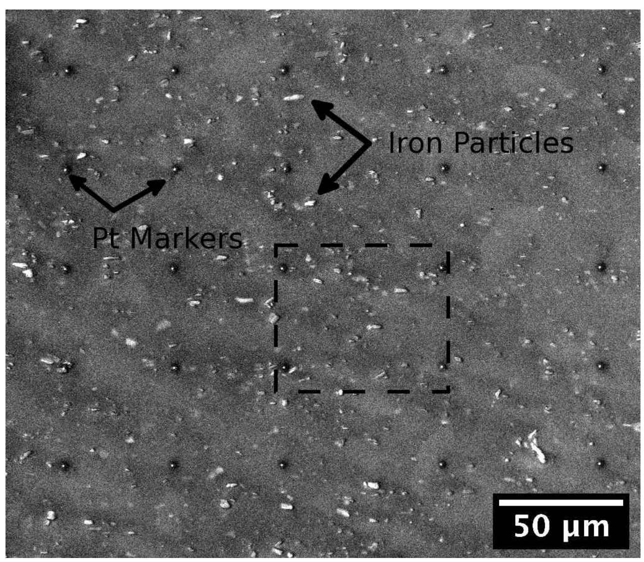

[**Fig 15** Pt alignment markers deposited on the surface of 1100-O Al tensile sample. These markers are used to align the EBSD FOV with the DIC FOV. An additional off-center marker exists outside of the image FOV to orient the EBSD data. The dashed box denotes the test FOV.]

The test was performed using an *in-situ* tension-compression stage (Kammrath & Weiss Tension/Compression Module) equipped with a 1 kN load cell and mounted within the FEI QUANTA 200 3D SEM chamber. SEM operating parameters were: 20kV accelerating voltage, 0.31 nA beam current, 13.1 mm working distance, image resolution of 33 nm/pixel (67.4 μm HFW), image size of 2048x1768 pixels, 10 microsecond dwell time, and 4x image integration. First, calibration images were captured of a patterned pure aluminum sample mounted to the Inconel calibration sample, after which the tensile sample was strained in tension at a displacement rate of 8 μm/second. The sample was loaded in steps and held at a constant global displacement during image capture. To capture initial strain localization, displacement steps of 8 μm (measured with a stage-mounted linear variable differential transformer) were used, corresponding to strain increments of 0.1%. Once localization in the test sample had developed, the displacement step was increased to 50 μms (0.625%). Throughout loading, additional calibration images of the unloaded calibration pattern were captured approximately every 30 minutes. This 30 minute spacing was originally chosen because it matched up well with drops in the chamber pressure readout, initially suspected as a cause of drift distortion. Later experiments at low vacuum variable pressure mode, and at different levels of vacuum in high vacuum mode, did not reveal a relationship between chamber pressure and drift. 30 minutes continues to be used since it typically yields ten additional drift distortion image pairs. This is a sufficient number of data points for an accurate quadratic drift velocity fit while also resulting in a much shorter test than those where image pairs are captured after every load step.

Post-test, images were first correlated using commercial software [21] with a subset size of 45 pixels and a step size of 1 pixel. Image distortions were then removed following the techniques described herein, after which strains were recalculated by fitting 15x15 data point subsets of the displacement fields with bi-cubic surface fits. A 15x15 data point subset was chosen because this subset size was determined to provide the most accurate match to the strain fields calculated by Vic-2D. The gradients of the bi-cubic surfaces were calculated and used to calculate the distortion-free Lagrangian finite strain tensors:

$$\varepsilon_{xx} = \frac{du}{dx} + \frac{1}{2}\left[\left(\frac{du}{dx}\right)^2 + \left(\frac{dv}{dx}\right)^2\right] \qquad (1)$$

$$\varepsilon_{yy} = \frac{dv}{dy} + \frac{1}{2}\left[\left(\frac{du}{dy}\right)^2 + \left(\frac{dv}{dy}\right)^2\right] \qquad (2)$$

$$\varepsilon_{xy} = \frac{1}{2}\left(\frac{du}{dy} + \frac{dv}{dx}\right) + \frac{1}{2}\left(\frac{du}{dx}\frac{du}{dy} + \frac{dv}{dx}\frac{dv}{dy}\right) \quad (3)$$

Note that the shear strain calculation used above assumes that the y-axis points upwards while in digital images, the y-axis points down. If data is presented using the digital image axis convention, the negative value of the shear strain should be used. The other strain fields are not affected by this axis rotation. In this experiment, the maximum observable distortions were -0.25 and -0.3 μms for drift distortion in the x- and y-directions respectively and -0.037 and 0.013 μms of spatial distortion in x- and y-directions respectively.

Results and Discussion

The EBSD inverse pole figure (IPF) map of the 1100-O Al tensile sample from the dashed box in figure 15 is shown in figure 16. As evident in figure 16, the test FOV is composed primarily of grains separated by high angle grain boundaries (HAGBs) possessing misorientations > 15° denoted by white lines. Data points with a confidence index less than 0.1 have been removed and appear as black points. These black data points represent the locations of iron intermetallic particles at the surface of the test sample that interfered with indexing Kikuchi patterns.

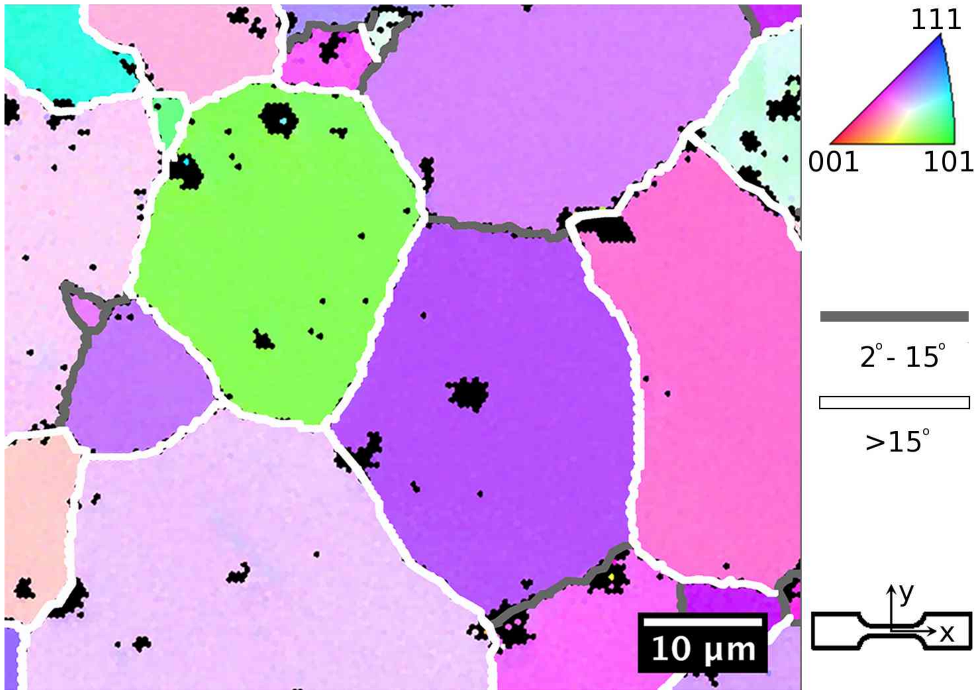

[**Fig 16** Inverse pole figure (IPF) map of the 1100-O aluminum tensile sample test FOV. Data points at iron intermetallic particles with confidence indices under 0.1 have been removed.]

As the sample was loaded, axial strain localization progressed as slip bands from grains that showed early localization into neighboring grains, as evident in the first column of images in figure 17. The evolution of the strain field clearly demonstrates how dislocation slip is able to proceed more easily in the favorably oriented grains than in neighboring grains with unfavorable orientations. As shown in the Schmid factor map in figure 18a, strain localization primarily appears in grains that possess a high Schmid factor and thus are oriented favorably for dislocation slip. Transverse strain, shown in the second column of figure 17, localized in bands and also concentrated at high angle grain boundaries. It is important to note that transverse strain localization is not apparent at the axial slip band localization in the grain marked 'I' in the axial strain fields of figure 17. This is due to the fact that these slip bands are nearly vertical, with slip occurring primarily in the x and z directions and not in the transverse y direction. However, transverse strain does localize with the slip bands observed in the axial strain field of the grain marked ‘II’ in figure 17. This suggests that the slip system is oriented so that displacements occur in both x and y. This is also confirmed by the shear strain localization at this location as seen in the shear strain fields of figure 17. Shear localization also appears in the grain marked ‘III’ in the shear strain fields of figure 17. Slip system activation is related to Schmid factor in this case, in contrast to observations in refs 7 and 8. This may be due to the fact that this experiment has a higher spatial resolution and all strain fields are examined.

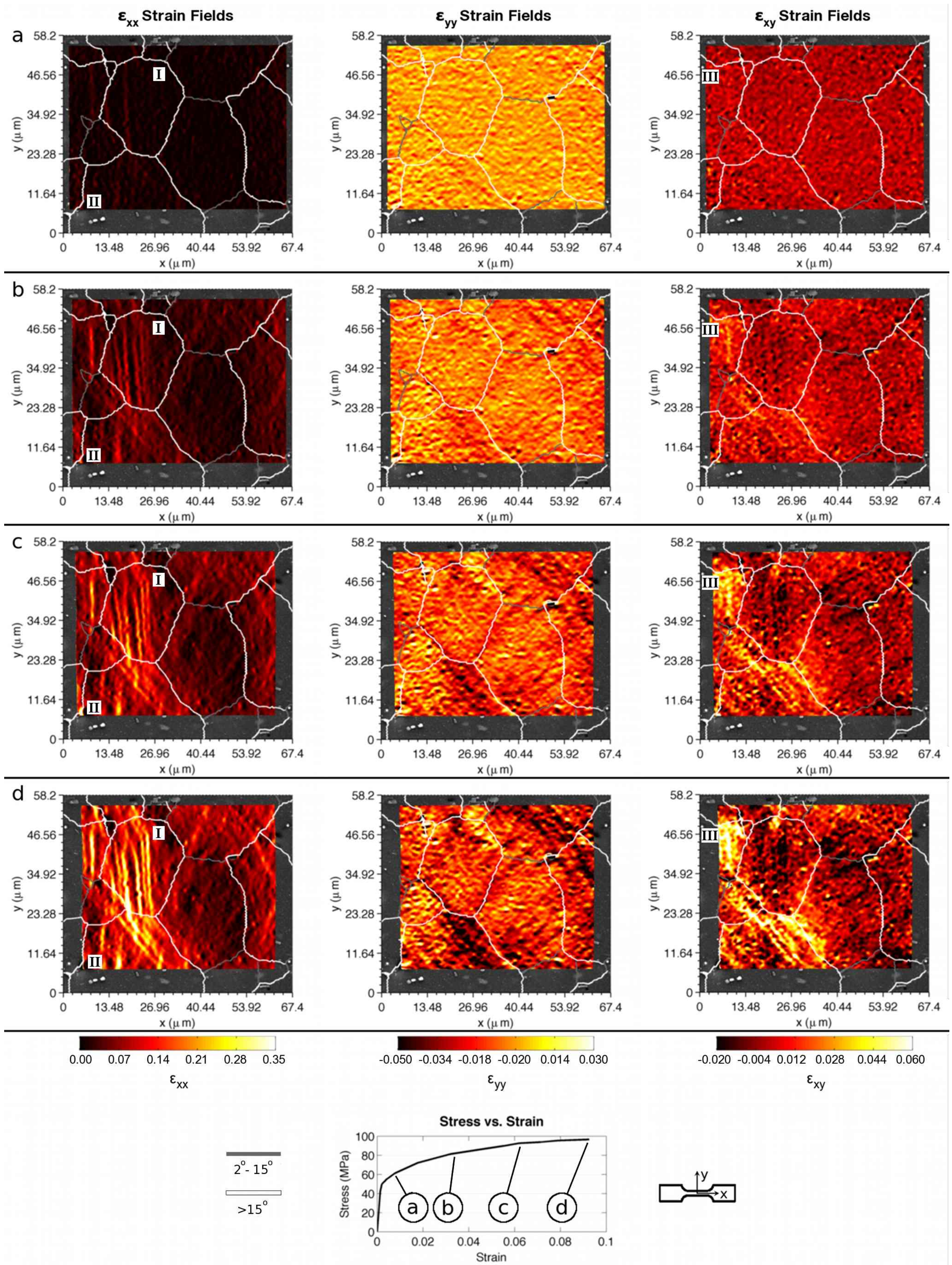
εxx Strain Fields
εyy Strain Fields
εxy Strain Fields
a
b
c
d
I
II
III
y (μm)
x (μm)
0.00 0.07 0.14 0.21 0.28 0.35
εxx
-0.050 -0.034 -0.018 -0.020 0.014 0.030
εyy
-0.020 -0.004 0.012 0.028 0.044 0.060
εxy
2°- 15°
>15°
Stress vs. Strain
Stress (MPa)
Strain
y
x

[**Fig 17** Axial, transverse, and shear strain fields for a tensile test on 1100-O Al at four different loads. HAGBs are represented by white lines, LAGBs are represented by grey lines. Strain is observed to localize at slip bands in grains oriented favorably for dislocation slip.]

Active slip planes were identified by careful alignment of the DIC strain field with the EBSD crystallographic data. Aluminum is a face centered cubic metal and deforms by dislocation slip on $\{111\}$ planes in the $<1\bar{1}0>$ directions. Dislocation slip will appear as localized strain in one of the strain fields depending on the orientation of the slip plane and slip direction. For example, slip will appear as axial strain localization if the slip plane is at a shallow angle to the sample surface and slip occurs primarily in the direction that tension is applied, as is the case with the active slip plane in the grain marked 'I' in figure 17. Figure 18b shows the axial strain field at the maximum load overlaid with lines representing $\{111\}$ plane traces of the slip systems possessing the highest Schmid factor in each grain. This figure confirms that strain localization is aligned with the $\{111\}$ plane traces and can be inferred to be a result of dislocation slip.

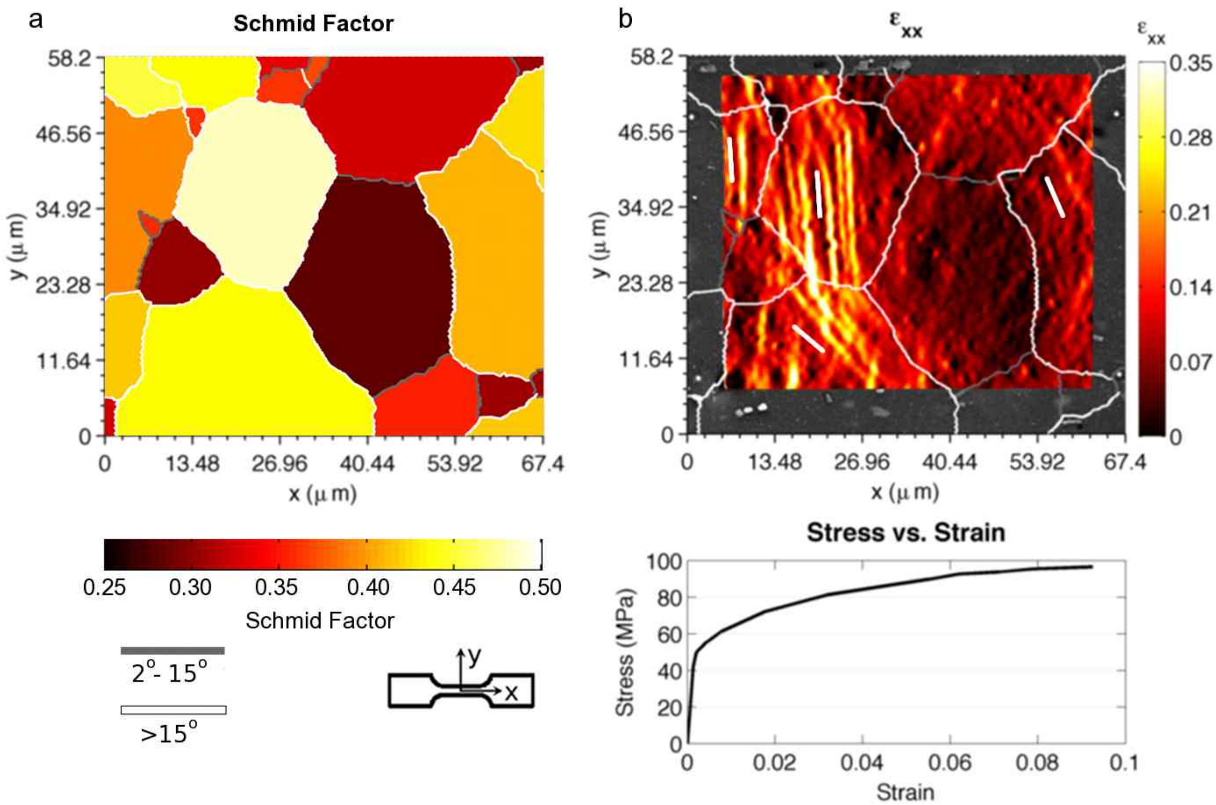

[**Fig 18** (a) shows the Schmid factor plot for the grains in the test FOV. (b) shows the axial strain field at maximum load overlaid with {111} plane traces of the slip systems possessing the highest Schmid factor. Short white lines represent {111} plane traces.]

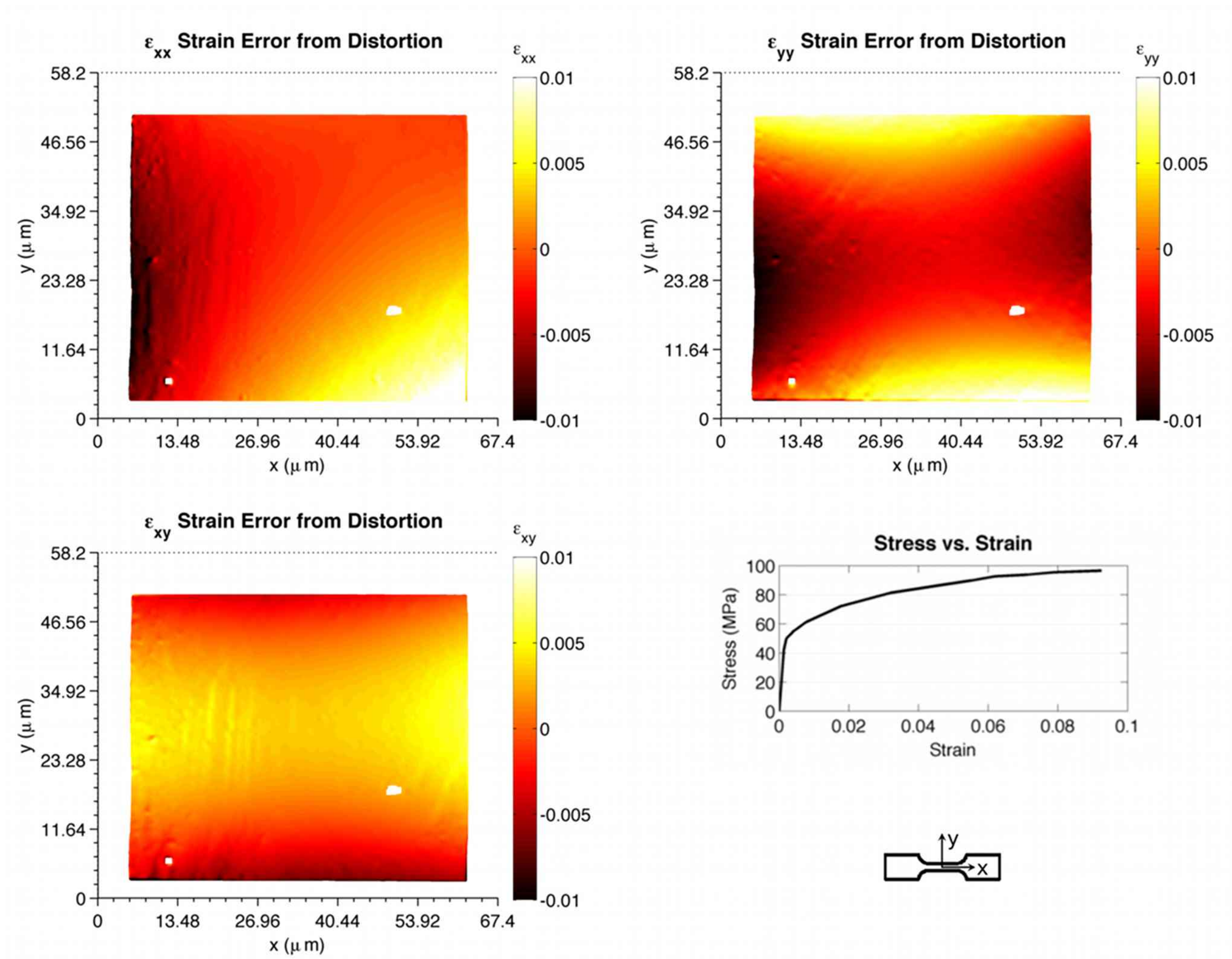

[**Fig 19** Errors in the strain fields resulting from image distortion. The curvature of the strain fields is primarily due to drift distortion (larger than spatial distortion in this test due to the relatively fine 33nm/pixel image resolution).]

At the maximum load reached during this test, image distortion incurred strain errors as high as 0.01 if left uncorrected. Figure 19 shows this error, calculated by subtracting the distorted strain fields from the distortion free strain fields. These errors are a result of both drift and spatial distortion. Drift distortion has a larger effect at the fine image resolution of 33 nm/pixel used in this experiment. Much of the curvature of these strain error surfaces are a result of drift distortion which had a magnitude as high as 0.3 μms in the final test image. Spatial distortion is affected by the amount of displacement at each data point. Thus, at slip bands where large displacements occur, spatial distortion is expected to be greater, which is confirmed to be the case. This high error is in contrast to the maximum error of 0.0035 observed in an experiment with an image resolution of 730 nm/pixel. That experiment experienced larger spatial distortion that was offset by the low drift distortion customary at that low magnification.

Conclusions

SEM-DIC is an emerging and powerful technique used to study nano- and micro-scale phenomena in a wide range of materials. By combining SEM-DIC with EBSD microstructure mapping, it is now possible to link *in-situ* deformation behavior, at the length scale of the microstructure, directly to the underlying crystallography of the material. SEM-DIC is a powerful new experimental technique, but its correct implementation introduces challenges that are far more complex than those encountered in macro-scale DIC.

- SEM image distortions can introduce significant error into SEM-DIC displacement fields. Drift distortion velocity as high as 0.34 pixels/minute for an image resolution of 29 nm/pixel and spatial distortion of 1.6 pixels for an image resolution of 730 nm/pixel at a strain of 0.2 were observed in this work. Drift distortion is more problematic at high magnification while spatial distortion dominates at low magnification. Spatial distortion at a point is related to the displacement that point experiences. Spatial distortion can be reduced by keeping the reference field of view centered throughout the test to prevent rigid body translations.
- Performing drift distortion corrections without accounting for stress relaxation can result in larger errors than if the data is left uncorrected. Two approaches are introduced to correctly account for stress relaxation. When SEM hardware modifications are possible, the use of a stationary unloaded calibration pattern is used to accurately remove stress relaxation induced displacements from calibration image data. A technique to relate stress

relaxation induced displacements to the load drop during image capture is presented as an alternate method when the addition of an unloaded calibration pattern to the in-SEM testing setup is infeasible.

- The impact of a wide range of SEM settings on image noise is quantified and noise minimization schemes are discussed, where it is shown that proper microscope settings can reduce noise in the SEM-DIC displacement fields to below that of a Point Grey Grasshopper, Model 50S5M/C-C CCD commonly used in optical DIC experiments. As a general guideline, high beam current (large spot size), long dwell time, and image integration should be utilized.
- The location of early strain localization was correctly determined by the application of an appropriate averaging filter to minimize noise inherent to the SEM imaging process. This results in averaged strain values and does not provide quantitative early strain measures.
- Active slip planes in 1100-O aluminum were identified by aligning the DIC strain field with the EBSD crystallographic data. As loading proceeded, axial strain localization progressed as slip bands from grains that showed early localization into neighboring grains. The evolution of the strain field clearly demonstrated how dislocation slip was able to proceed much more easily in favorably oriented grains than in neighboring grains with unfavorable orientations.
- Transverse and shear strain localized in bands and also concentrated at grain boundaries. Transverse strain localization was not apparent in a grain where the slip bands were nearly vertical, with slip occurring primarily in the x and z directions and not in the y direction. Shear strain localized at HAGBs suggesting imperfect slip transfer across the boundary as a result of high misorientation.

- In this test, image distortions were shown to result in strain errors as high as 0.01 if left uncorrected.

Acknowledgements

This work was supported by the National Science Foundation under Grant No. 092753 and by the Rackham Graduate School Non-Traditional Student Fellowship from the University of Michigan. We also gratefully acknowledge funding from the US Department of Energy, Office of Basic Energy Sciences (contract No. DE-SC0003996 monitored by Dr. John Vetrano) who supported portions of the distortion correction computational work. Portions of this work were performed at the Electron Microbeam Analysis Laboratory (EMAL) at the University of Michigan.

References

[1] Sutton MA, Wolters WJ, Peters WH, Ranson WF, McNeill SR (1983) Determination of displacements using an improved digital correlation method, Image and Vision Computing 1, pp. 133-139, 10.1016/0262-8856(83)90064-1.

[2] Peters WH, Ranson WF (1982) Digital imaging techniques in experimental stress analysis, Optical Engineering 21, pp. 427–431, 10.1117/12.7972925.

[3] Sutton MA, Orteu JJ, Schreier HW (2009) Digital image correlation (DIC). In: Image Correlation for Shape, Motion and Deformation Measurements (Springer US) p. 83, 10.1007/978-0-387-78747-3 5.

[4] Schwarzer RA, Field DP, Adams BL, Kumar M, Schwartz AJ (2009) Present state of electron backscatter diffraction and prospective developments, in: Schwartz AJ, Kumar M, Adams BL, Field DP (Eds.), Electron Backscatter Diffraction in Materials Science, (Springer US) pp. 1–20, 10.1007/978-0-387-88136-2_1.

[5] Maitland T, Sitzman S (2006) Backscattering detector and EBSD in nanomaterials characterization, in: Zhou W, Wang Z (Eds.), Scanning Microscopy for Nanotechnology, (Springer New York) pp. 41–75, 10.1007/978-0-387-39620-0_2.

[6] Dautriat J, Bornert M, Gland N, Dimanov A, Raphanel J (2011) Localized deformation induced by heterogeneities in porous carbonate analysed by multi-scale digital image correlation, Tectonophysics 503, pp. 100-116, 10.1016/j.tecto.2010.09.025.

[7] Tschopp MA, Bartha BB, Porter WJ, Murray PT, Fairchild SB (2009) Microstructure-dependent local strain behavior in polycrystals through In-Situ scanning electron microscope tensile experiments, Metallurgical and Materials Transactions A 40, pp. 2363–2368, 10.1007/s11661-009- 9938-6.

[8] Walley JL, Wheeler R, Uchic MD, Mills MJ (2012) In-Situ mechanical testing for characterizing strain localization during deformation at elevated temperatures, Experimental Mechanics 52, pp. 405–416, 10.1007/s11340- 011-9499-7.

[9] Kammers AD, Daly S (2011) Small-scale patterning methods for digital image correlation under scanning electron microscopy, Measurement Science and Technology 22, 125501, 10.1088/0957-0233/22/12/125501

[10] Kammers, A. D., & Daly, S. (2012). Self-Assembled Nanoparticle Surface Patterning for Improved Digital Image Correlation in a Scanning Electron Microscope, Experimental Mechanics, 10.1007/s11340-013-9734-5.

[11] Sutton MA, Li N, Garcia D, Cornille N, Orteu JJ, McNeill SR, Schreier HW, Li X (2006) Metrology in a scanning electron microscope: theoretical developments and experimental validation, Measurement Science and Technology 17 pp. 2613-2622, 10.1088/0957-0233/17/10/012.

[12] Sutton MA, Li N, Joy DC, Reynolds AP, Li X (2007) Scanning electron microscopy for quantitative small and large deformation measurements part I: SEM imaging at magnifications from 200 to 10,000. Experimental Mechanics 47, pp 775–787, 10.1007/s11340-007- 9042-z.

[13] Sutton MA, Li N, Garcia D, Cornille N, Orteu JJ, McNeill SR, Schreier HW, Li X, Reynolds AP (2007) Scanning electron microscopy for quantitative small and large deformation measurements part II: Experimental validation for magnifications from 200 to 10,000. Experimental Mechanics 47, pp 789–804, 10.1007/s11340-007-9041-0.

[14] Joy DC, Noise and its effects on the low-voltage SEM (2008) in: Schatten H, Pawley JB (Eds.), Biological Low-Voltage Scanning Electron Microscopy, Springer New York, pp. 129–144, 10.1007/978-0-387- 72972-5 4.

[15] Kuo YH, Wu CJ, Yen JY, Chen SY, Tsai KY, Chen YY (2011) Silicon photodiodes for electron beam position and drift detection in scanning electron microscopy and electron beam lithography system, Nucl Instrum Meth A 645, pp 84-89, 10.1016/j.nima.2010.12.227.

[16] Goodberlet JG, Hastings JT, Smith HI (2001) Performance of the Raith 150 electron-beam lithography system, J. Vac. Sci. Technol. B 19, 2499-2503, 10.1116/1.1414018.

[17] Chen SY, Tsai KY; Ng PCW, Ng HT, Liu CH, Shen YT, Kuan CH, Chen YY, Kuo YH, Wu CJ, Yen JY (2011) In situ beam drift detection using a two-dimensional electron-beam position monitoring system for multiple-electron-beam–direct-write lithography, J Vac Sci Technol B 29 pp.041607-1-041607-12, 10.1116/1.3613697.

[18] Smith HI, Hector SD, Schattenburg ML, Anderson EH (1991) A new approach to high fidelity e-beam and ion-beam lithography based on an in situ global-fiducial grid, J. Vac. Sci. Technol. B 9, pp. 2992-2995, 10.1116/1.585355.

[19] Ogasawara M, Ohtoshi K, Sugihara K (1995) Reduction of Electron Beam Drift Caused by Deflecting Electrode by Downflow Cleaning Process, Jpn. J. Appl. Phys. 34, pp. 6655-6657, 10.1143/JJAP.34.6655.

[20] Ando A, Sunaoshi H, Sato S, Magoshi S, Hattori K, Suenaga M, Wada H, Housai H, Hashimoto S, Sugihara K (1996) Contamination Charging up Effect in a Variably Shaped Electron Beam Writer, Jpn. J. Appl. Phys. 35, pp. 6426-6428, 10.1143/JJAP.35.6426.

[21] Vic-2D (2009) [software]. Columbia SC, USA: Correlated Solutions Inc.

[22] Rohde RW, Jones WB, Swearengen JC (1981) Deformation modeling of aluminum: Stress relaxation, transient behavior, and search for microstructural correlations, Acta Metallurgica 29, pp. 41-52, 10.1016/0001-6160(81)90085-7.

[23] Lee HJ, Cornella G, Bravman JC (2000) Stress relaxation of free-standing aluminum beams for microelectromechanical systems applications, Applied Physics Letters 76, pp. 3415–3417, 10.1063/1.126664.

[24] Nowick AS, Berry BS (1972) Anelastic relaxation in crystalline solids, Academic Press, New York.

[25] Schreier HW, Braasch JR, Sutton MA (2000) Systematic errors in digital image correlation caused by intensity interpolation, Optical Engineering 39, pp. 2915–2921, 10.1117/1.1314593.

[26] ASTM Standard E8, 2011, "Standard Test Methods for Tension Testing of Metallic Materials," ASTM International, West Conshohocken, PA, 2011, www.astm.org.